This is a “preproof” accepted article for *Annals of Glaciology*.

This version may be subject to change during the production process.

10.1017/aog.2024.47

Bragg scattering of surface-gravity waves by an ice shelf with rolling surface morphology

Yuri V. Konovalov

ORCID: 0000-0002-8469-9706

Department of Mathematics, MIREA - Russian Technological University, Vernadsky avenue 78, Moscow, Russian Federation, 119454

Correspondence to: Y.V. Konovalov (yu-v-k@yandex.ru)

ABSTRACT

The propagation of elastic-flexural gravity waves through an ice shelf is modeled by full 3-D elastic models that are coupled to a treatment of under-shelf sea-water flux: (i) finite-difference model (Model 1); (ii) finite-volume model (Model 2); (iii) depth-integrated finite-difference model (Model 3). The sea water flow under the ice shelf is described by a wave equation involving the pressure (the sea water flow is treated as a "potential flow"). Numerical experiments were undertaken for an ice shelf with "rolling" surface morphology, which implies a periodic structure of the ice shelf. The propagation of ocean waves through an ice shelf with rolling surface morphology is accompanied by Bragg scattering (also called Floquet band insulation). The numerical experiments reveal that band gaps resulting from this scattering occur in the dispersion spectra in frequency bands that are consistent with the Bragg's law. Band gaps render the medium opaque to wave, i.e., essentially, the abatement of the incident ocean wave by ice shelf with rolling surface morphology is observed in the models. This abatement explains the ability of preserving of ice shelves like Ward Hunt Ice Shelf, Ellesmere Island, Canadian Arctic, from the possible resonant-like destroying impact of ocean swell.

Keywords: ice shelf vibrations, Bragg scattering, under-shelf sea-water flux, ice shelf with periodic structure, "rolling" morphology of the ice surface, abatement of incident ocean wave

INTRODUCTION

The Ward Hunt (west) Ice Shelf located near Ward Hunt Island ($83^0\ 6'\ 0''\ N; 74^0\ 10'\ 0''\ W$), on the north coast of Ellesmere Island, Nunavut, Canada, constitutes a ~ 50 m thick rim of land-fast multi-year marine ice. The Ward Hunt Ice Shelf is not strictly an ice shelf in the sense commonly used in reference to Antarctic ice shelves, because it originates as multi-year land fast sea ice that has become immobile to the point of no longer drifting with wind and ocean current (Dowdeswell and Jefferies, 2017). Owing to this immobility, the Ward Hunt Ice Shelf represents a secure floating platform that allows observation of sea swell and other types of surface gravity waves (e.g., impulsive waves generated from ridging, thermal fracturing, “micro tsunamis” generated by ice-cliff calving, etc.) using broadband seismometers (Cathles and others, 2009). The concept of using ice-shelf platforms as observatories for sea swell in sea-ice covered waters is well supported in various Antarctic examples (e.g., Cathles and others, 2009; Bromirski and others, 2015; Cannata and others, 2019); however, the concept has never been tried before on ice shelves that fringe the Canadian Archipelago and Greenland. Seismometers have been deployed on embayed sea ice, for example in Svalbard; however, these deployments are at risk due to sea-ice breakup and drift (e.g., Serripierri and others, 2022).

Broadband seismographs deployed on floating ice shelves have the ability to observe a variety of oceanic and sea-ice phenomena including sea swell (both locally generated and trans oceanic (Cathles and others, 2009; Tsai and McNamara, 2011), hydro acoustic signals (tremor) generated by colliding icebergs and sea ice floes (MacAyeal and others, 2008), impulsive waves generated by iceberg calving and sea-ice ridging (MacAyeal and others, 2009), ice quakes associated with sea-ice deformation, and thermal fracturing of sea ice (Lewis and others, 1994) and superimposed ice layers (MacAyeal and others, 2019). In recent years, these observations have been used to demonstrate how seismological observation can define conventional properties such as sea-ice concentration and thickness (Cannata and others, 2019), as well as to infer difficult to observe properties such as depth of snow superimposed on sea ice (e.g., Chaput and others, 2018; Schlindwein and others, 2020; Serripierri and others, 2022; Guillemot and others, 2021). An example of ice-shelf deployed seismic data can be found in (Cathles and others, 2009).

The surface elevation of the now-diminished Ellesmere Ice Shelf and the Ward Hunt Ice Shelf consists of periodic waves, called “rolls” by the European explorers who first described them (Hattersley-Smith and others, 1955; Hattersley-Smith, 1957), that have an amplitude of meters and wavelength of hundreds of meters. Rolls are rarely found on ice shelves of the Antarctic, and only in limited areas, not the pervasive full coverages seen on the Ward Hunt Ice Shelf. Their origin is unknown, and many hypotheses have been offered to explain them (Jeffries, 2017; Coffee and others, 2022). Whatever their origin, the fact that they dominate an ice shelf that grew from multi-year sea ice in the Last Ice Area, a region in the high latitudes of the Canadian Arctic and Greenland (e.g. Newton and others, 2021), demands attention. A hypothesis that we put forward is that the rolling surface morphology, created by whatever mechanism, offers an advantage to the survival of the multi-year sea ice which has this morphology. Specifically, the periodic variation of ice thickness creates ‘band gaps’, or frequency bands which prohibit the propagation of air- and water-coupled flexural gravity waves (Freed-Brown and others, 2012; Nekrasov and MacAyeal, 2023). If the right frequencies of waves are prohibited from propagating through the ice shelf (they will be reflected at the ice front), it is possible that the band gap will protect the ice shelf from wave-flexure induced damage and fracture.

The propagation of elastic-flexural waves through an ice shelf can be modeled by elastic models (e.g. Holdsworth and Glynn, 1978, in addition to many others), based on elastic thin plate / elastic beam approximations. There are models among these that consider coupled ice-shelf / sub-ice shelf cavity systems (Holdsworth and Glynn, 1978; Sergienko, 2013, 2017; Papathanasiou and others, 2015, 2019; Meylan and others, 2017; Ilyas and others, 2018; Kalyanaraman and others, 2019, 2020; McNeil and Meylan 2023; Bennetts and others, 2024) and permit estimation of possible effects of tides and ocean swell actions on the calving process. In particular, these models consider the eigenvalue problem for the ice-shelf / sub-ice sea water systems (Holdsworth and Glynn, 1978; Papathanasiou and others, 2019), which is of interest in terms of possible resonances in the system. Further advancement of elastic-beam models occured in the direction of visco-elastic rheological model development. In particular, tidal flexure of an ice-shelf was obtained using the linear visco-elastic Burgers model (Reeh and others, 2003; Walker and others, 2013), nonlinear thin-plate visco-elastic model (MacAyeal and others, 2015) and the nonlinear 3D visco-elastic full-Stokes model (Rosier and others, 2014). In particular, visco-elastic modeling provides a way (i) to explain the observed tidal flexure data; (ii) to explain ice-shelf response to sudden changes of surface loads and applied bending moments (e.g. draining supraglacial lakes, iceberg calving, surface and basal crevassing).

Investigation of modeled dispersion spectra reveals that the spectra obtained for an ice shelf with crevasses can be qualitatively different from the spectra in the case of no crevasses (Freed-Brown and others, 2012). Crevasses are widely distributed features in all ice shelves, and their appearance, growth and penetration is the subject of many studies (e.g. Van der Veen, 1998, 2002; Scambos and others, 2000). Essentially, the dispersion spectra obtained for a crevasse-ridden ice shelf reveal “band gaps” that are absent from the spectra obtained for an ice shelf without crevasses. These band gaps are the frequency ranges over which no eigenmodes exist (Freed-Brown and others, 2012) and are a phenomenon which emerges when a wave is propagated through periodic structure (Sheng, 2006). Band gaps arise in many different systems, including crystallography, photonic crystals, electron transport in metals and semiconductors (Ashcroft and Mermin, 1976), the formation of nearshore underwater sandbars (Mei, 1985), and gravity wave propagation through periodical structures of floating ice (Chou, 1998; Bennetts and others, 2009; Bennets and Squire, 2009; Bennets and Williams, 2010; Bennets and Squire, 2012).

In this study the propagation of elastic-flexural waves through an ice shelf with rolling surface morphology (Ward Hunt Ice Shelf morphology) was modeled by full 3-D finite-difference elastic models that are coupled to a treatment of under-shelf sea-water motion. These models differ in their approximation of the momentum equations: (i) Model 1 is based on the known differential form of the momentum equations and on the finite-difference approximation of the momentum equations (Konovalov, 2020, 2021b); (ii) Model 2 is based on the integral form of the momentum equations and the approximation of this form by the finite-volume method (Konovalov, 2023b, 2023c); (iii) Model 3 (Konovalov, 2021c) is based on the integro-differential form of the momentum equations and on a finite-difference approximation of this form (in this model the depth integration does not imply a thin plate approximation). In all three of these models, seawater under the ice shelf is treated as a homogeneously dense fluid, and the flow of water under ice shelf as is treated as a "potential flow". The sea water motion in all developed models is described by a wave equation involving the pressure, and couples to the elastic motions of the ice through the pressure at the ice/water interface (Holdsworth and Glynn, 1978).

Numerical experiments show that "rolling" surface morphology of the ice shelf, a distinctive feature of Arctic ice shelves along Ellesmere Island, can have a profound effect on how elastic-flexural waves propagate through the system. The experiments show that rolling surface morphology produces Bragg scattering (also called Floquet band insulation) that is potentially effective in preventing an incident wave from entering the ice shelf and causing subsequent fracture damage. The numerical results show frequency band gaps (band insulation) that are consistent with the Bragg's law. The numerical results further show that these band gaps render the ice shelf/ocean system opaque to wave propagation with frequencies that fall within the range of the band gaps. By abating incident ocean wave activity, the rolling surface morphology inadvertently provides a fitness to the ice shelf that protects it from damage.

FIELD EQUATIONS

The 3D elastic model is based on the well-known momentum equations (e.g. Landau and Lifshitz, 1986; Lurie, 2005):

$$\begin{cases} \dfrac{\partial \sigma_{xx}}{\partial x} + \dfrac{\partial \sigma_{xy}}{\partial y} + \dfrac{\partial \sigma_{xz}}{\partial z} = \rho \, \dfrac{\partial^2 U}{\partial \, t^2}; \\ \dfrac{\partial \sigma_{yx}}{\partial x} + \dfrac{\partial \sigma_{yy}}{\partial y} + \dfrac{\partial \sigma_{yz}}{\partial z} = \rho \, \dfrac{\partial^2 V}{\partial \, t^2}; \\ \dfrac{\partial \sigma_{zx}}{\partial x} + \dfrac{\partial \sigma_{zy}}{\partial y} + \dfrac{\partial \sigma_{zz}}{\partial z} = \rho \, \dfrac{\partial^2 W}{\partial t^2} + \rho g; \\ 0 < x < L; y_1(x) < y < y_2(x); \; h_b(x,y) < z < h_s(x,y), \end{cases} \tag{1}$$

where (XYZ) is a rectangular coordinate system with x-axis along the central line (in the direction of wave propagation), and z-axis is pointing vertically upward; U, V and W are two horizontal and one vertical ice displacements, respectively; $\boldsymbol{\sigma}$ is the stress tensor; and ρ is ice density. The ice shelf is of length L along the central line. The geometry of the ice shelf is assumed to be given by lateral boundary functions $y_{1,2}(x)$ at sides labeled 1 and 2 and functions for the surface and base elevation, $h_{s,b}(x,y)$, denoted by subscripts s and b, respectively. Thus, the domain on which Eqs. (1) are solved is $\Omega = \{0 < x < L,\ y_1(x) < y < y_2(x),\ h_b(x,y) < z < h_s(x,y)\}$.

Equations (1) can be rewritten in integro-differential form. This integro-differential form results from the vertical integration of the momentum equations (1) from the current vertical coordinate to the ice surface. In particular, considering the first equation from (1) and integrating over z' from the current z-coordinate to h_s we obtain the equation

$$\int_z^{h_s} \frac{\partial \sigma_{xx}}{\partial x}\, dz' + \int_z^{h_s} \frac{\partial \sigma_{xy}}{\partial y}\, dz' + \sigma_{xz}|_{z=h_s} - \sigma_{xz} = \rho \int_z^{h_s} \frac{\partial^2 U}{\partial t^2} dz' \tag{2}$$

Next, using the Leibniz integral rule, we replace the first and second terms in equation (2) with the following, respectively

$$\int_z^{h_s} \frac{\partial \sigma_{xx}}{\partial x}\, dz' = \frac{\partial}{\partial x} \int_z^{h_s} \sigma_{xx}\, dz' - (\sigma_{xx})_{z=h_s} \frac{\partial h_s}{\partial x}; \tag{3.1}$$

$$\int_z^{h_s} \frac{\partial \sigma_{xy}}{\partial y}\, dz' = \frac{\partial}{\partial y} \int_z^{h_s} \sigma_{xy}\, dz' - \left(\sigma_{xy}\right)_{z=h_s} \frac{\partial h_s}{\partial y}. \tag{3.2}$$

Thus, instead of equation (2) we obtain the following equation

$$\frac{\partial}{\partial x} \int_z^{h_s} \sigma_{xx}\, dz' + \frac{\partial}{\partial y} \int_z^{h_s} \sigma_{xy}\, dz' - (\sigma_{xx})_{z=h_s} \frac{\partial h_s}{\partial x} - \left(\sigma_{xy}\right)_{z=h_s} \frac{\partial h_s}{\partial y} + (\sigma_{xz})_{z=h_s} - \sigma_{xz} = \rho \int_z^{h_s} \frac{\partial^2 U}{\partial t^2} dz'. \tag{4}$$

Taking in to account that the expression $\frac{-(\sigma_{xx})_{z=h_s}\frac{\partial h_s}{\partial x} - \left(\sigma_{xy}\right)_{z=h_s}\frac{\partial h_s}{\partial y} + (\sigma_{xz})_{z=h_s}}{\sqrt{\left(\frac{\partial h_s}{\partial x}\right)^2 + \left(\frac{\partial h_s}{\partial y}\right)^2 + 1}}$ is the x-component of the force acting on a unit square of the ice surface (e.g. Landau and Lifshitz, 1986) and it is equal to zero accordingly the boundary conditions (ice surface is stress free), we finally obtain the following equation

$$\frac{\partial}{\partial x}\int_{z}^{h_s}\sigma_{xx}\,dz' + \frac{\partial}{\partial y}\int_{z}^{h_s}\sigma_{xy}\,dz' - \sigma_{xz} = \rho\int_{z}^{h_s}\frac{\partial^2 U}{\partial t^2}dz'. \tag{5}$$

Performing similar manipulations with the second and third equations from (1), we obtain the following equations

$$\frac{\partial}{\partial x}\int_{z}^{h_s}\sigma_{yx}\,dz' + \frac{\partial}{\partial y}\int_{z}^{h_s}\sigma_{yy}\,dz' - \sigma_{yz} = \rho\int_{z}^{h_s}\frac{\partial^2 V}{\partial t^2}dz' \tag{6}$$

and

$$\frac{\partial}{\partial x}\int_{z}^{h_s}\sigma_{xx}\,dz' + \frac{\partial}{\partial y}\int_{z}^{h_s}\sigma_{zy}\,dz' - \sigma_{zz} = \rho g(h_s - z) + \rho\int_{z}^{h_s}\frac{\partial^2 W}{\partial t^2}dz'. \tag{7}$$

Thus, combining equations (5) – (7), we obtain the depth-integrated momentum equations, which are expressed as

$$\begin{cases} \frac{\partial}{\partial x}\int_{z}^{h_s}\sigma_{xx}dz' + \frac{\partial}{\partial y}\int_{z}^{h_s}\sigma_{xy}dz' - \sigma_{xz} = \rho\int_{z}^{h_s}\frac{\partial^2 U}{\partial t^2}dz'\,; \\ \frac{\partial}{\partial x}\int_{z}^{h_s}\sigma_{yx}dz' + \frac{\partial}{\partial y}\int_{z}^{h_s}\sigma_{yy}dz' - \sigma_{yz} = \rho\int_{z}^{h_s}\frac{\partial^2 V}{\partial t^2}dz'\,; \\ \frac{\partial}{\partial x}\int_{z}^{h_s}\sigma_{zx}dz' + \frac{\partial}{\partial y}\int_{z}^{h_s}\sigma_{zy}dz' - \sigma_{zz} = \rho g(h_s - z) + \rho\int_{z}^{h_s}\frac{\partial^2 W}{\partial t^2}dz'\,; \\ 0 < x < L; y_1(x) < y < y_2(x);\ h_b(x,y) < z < h_s(x,y). \end{cases} \tag{8}$$

Similar manipulations, for example, yield equations describing ice flow in a 2D ice-flow model (Pattyn, 2000, 2002).

Sub-ice water flow is described by the wave equation (Holdsworth and Glynn, 1978):

$$\frac{\partial^2 W_b}{\partial\, t^2} = \frac{1}{\rho_w}\frac{\partial}{\partial\, x}\left(d_0\frac{\partial\, P\prime}{\partial\, x}\right) + \frac{1}{\rho_w}\frac{\partial}{\partial\, y}\left(d_0\frac{\partial\, P\prime}{\partial\, y}\right), \tag{9}$$

where ρ_w is sea water density; $d_0(x,y)$ is the depth of the sub-ice water layer; $W_b(x,y,t)$ is the vertical deflection of the ice-shelf base, and $W_b(x,y,t) = W(x,y,h_b(x,y),t)$; and $P'(x,y,t)$ is the deviation of the sub-ice water pressure from the hydrostatic value.

The boundary conditions to the ice shelf are: (i) a stress free ice surface; (ii) the normal stress exerted by seawater at the ice-shelf free edges and at the ice-shelf base; and (iii) rigidly fixed edges at the grounding line of the ice-shelf. Moreover, the linear combination of the boundary conditions (Konovalov, 2019) also was applied in the models considered in this study. This linear combination is expressed as

$$\alpha_1 F_i(U,V,W) + \alpha_2 \Phi_i(U,V,W) = 0, \ i = 1,2,3, \tag{10}$$

where:

(i) $F_i(U,V,W) = 0$ is the typical form of the boundary conditions, i.e. $\sigma_{ik} n_k = f_i$ where, f_i is given forcing on the boundary ($\vec{n}$ is the unit vector normal to the surface);

(ii) $\Phi_i(U,V,W) = 0$ is the approximation based on integration of the typical form of the boundary conditions to the momentum equations (Eqs (1) or Eqs (8));

(iii) the coefficients α_1 and α_2 satisfy the condition $\alpha_1 + \alpha_2 = 1$.

The boundary conditions to the sea water layer correspond to the frontal incident wave. They are

(i) at $x = 0$: $\frac{\partial P\prime}{\partial x} = 0$;

(ii) at $y = y_1, y = y_2$: $\frac{\partial P\prime}{\partial y} = 0$;

(iii) at $x = L$: $P' = A_0\, \rho_w g\, e^{i\omega t}$, where A_0 is the amplitude of the incident wave.

The full description of **Model 1** based on equations (1), is presented in (Konovalov, 2019, 2020 2021a, 2021b). **Model 2** is based on the finite volume method of approximation of momentum equations (1) and is presented in (Konovalov, 2023b, 2023c). The full description of **Model 3** based on equations (8), is presented in (Konovalov, 2021c, 2023a).

MODEL SET-UP

The numerical experiments with forced vibrations were undertaken for a physically idealized ice shelf with the geometry shown in Figure 1. In the undeformed ice shelf, the four edges had coordinates $x = 0, x = L,\ y_1 = 0,\ y_2 = B$, where L is the plate length along the x-axis and B is the plate width along the y-axis ($B = y_2 - y_1$, see Eq. (1)).

The ice plate had only one fixed edge (at $x = 0$), while the other edges (at $x = L, y_1 = 0, y_2 = B$) were free. This is the special case of an ice shelf, which is also known as an "ice tongue" (e.g. Holdsworth and Glynn, 1978). The intact ice tongue was 2 km in longitudinal extent, 0.1-0.2 km width.

The "rolling" surface morphology (Coffey and others, 2022) was modeled by sinusoidally varying ice thickness

$$H(x) = H_0 + A_H \frac{\rho_w}{\rho} \cos\left(\frac{2\pi x}{\Delta l_r}\right), \tag{11}$$

where A_H is the amplitude of ice thickness oscillations, which was considered as a parameter of the models; Δl_r is the spatial periodicity of the "rolls" (Δl_r in the models was equal to 0.5 km); H_0 in the models was equal to 25m. Essentially, this ice tongue was considered as a part of the Ward Hunt Ice Shelf.

Taking into account the hydrostatic balance, the elevation of the ice surface $h_s(x, y)$ and the elevation of the ice base $h_b(x, y)$ are determined by the following equations, respectively:

$$h_s(x, y) = H\left(1 - \frac{\rho}{\rho_w}\right), \tag{12.1}$$

$$h_b(x, y) = -H\frac{\rho}{\rho_w}, \tag{12.2}$$

where H is the ice thickness (11).

That is, on the Ward Hunt Ice Shelf, both the ice surface and the ice base also had sinusoidal changes along the centerline (Figure 1).

The water-layer depth in the case of the intact ice tongue also had sinusoidal variation (Figure 1). The periodic structure of the ice tongue is expected to provide Bragg scattering if the double spatial periodicity of the rolls $2\,\Delta l_r$ is a multiple of the wavelength λ. Respectively, the Bragg wavenumbers $k_b^{(n)}$, at which we expect to observe band gaps in the modeled dispersion spectra, are expressed as

$$k_b^{(n)} = \frac{\pi\, n}{\Delta l_r},\ n = 1,2,\ldots \qquad (13)$$

In all performed experiments, the physical properties of ice were defined by the following values: Young's modulus *E=9GPa*, Poisson's ratio is equal to *0.33* (Schulson, 1999).

NUMERICAL EXPERIMENTS

Numerical experiments were carried out using three models with different combinations of parameters α_1 and α_2 in equation (10). The results presented below were obtained using **Model 1** for (i) $\alpha_1 = 1;\ \alpha_2 = 0$ and (ii) $\alpha_1 = 0.2;\ \alpha_2 = 0.8$; using **Model 2** for (i) $\alpha_1 = 1;\ \alpha_2 = 0$ and (ii) $\alpha_1 = 0;\ \alpha_2 = 1$; and using **Model 3** for $\alpha_1 = 1;\ \alpha_2 = 0$.

The **supplemental file** contains the results obtained from the experiments performed using Model 1 and Model 3. Here are the results obtained using Model 2.

Figure 2 shows vertical deflections of the ice shelf. In general, using the second type of boundary conditions ($\Phi_i(U, V, W)$ in equation (10)), the modeling reveal that the deflections are a superposition of a pure bending mode (Lamb-type mode) and a pure torsion mode (Figure 2b). By determining the distances between the maxima/minima along the centerline deflection profile and then determining the average value, we obtain the wavelength and, accordingly, the wavenumber for a given periodicity T ($T = \frac{2\pi}{\omega}$, where ω is the frequency of the forcing). Thus, we successively obtain a dispersion curve – the dependence of the wavenumber on the periodicity (or frequency) of the forcing (Figure 3).

In Figure 3, dispersion curve 1 was obtained for the ice shelf with constant ice thickness (the case of $A_H = 0$). In this case, the dispersion curve consists of sections of monotonic decrease, which are separated by inter-mode spaces (Figure 3) accompanying the transitions from the $n + 1$ to the n bending Lamb-type mode. In the case of the rolling periodic geometry of the ice shelf (Figure 1), the models yield the dispersion curves that have sections, where the typical relationship with monotonic decrease and inter-mode spaces is disturbed, as in dispersion curve 2 in Figure 3. In Figure 3, this section of curve 2 is the band gap, which occurs due to Bragg scattering and corresponds to the second Bragg wavenumber $k_b^{(2)} \approx 12.57\ km^{-1}$. Essentially, these sections with disturbed wavenumber values are defined by comparison with the typical relationship (curve 1 in Figure 3).

Experiments with ice shelves that have "rolling" surface morphology revealed that there is the threshold value of the amplitude of ice thickness oscillations (A_H in equation (11)), at which the band gaps appear in the dispersion spectra (Figure 4a) (Konovalov, 2023a). Essentially, the amplitude of ice thickness oscillations (A_H) determines the depth of cavities at the base of the ice shelf that result from the "rolling" morphology. These cavities are analogous to crevasses at the ice shelf base (Freed-Brown and others, 2012).

In Model 2, as in Model 1, the threshold value also depends on the *Bragg wavenumber*. The first band gap ($k_b^{(1)} \approx 6.28\ km^{-1}$), appears in the spectrum at $A_H > 14\ m$ (Figure 4a), i.e. the first threshold value $(A_H)_{th}^{(1)} \approx 14m$. The second band gap ($k_b^{(2)} \approx 12.57\ km^{-1}$), the third band gap ($k_b^{(3)} \approx 19.04\ km^{-1}$) and the fourth band gap ($k_b^{(4)} \approx 25.13\ km^{-1}$) appear in the spectrum at $A_H > 1\ m$ (Figure 4,b and 4,c), i.e. the corresponding threshold values $(A_H)_{th}^{(i)} \leq 1m; i = 2,3,4$.

As in Model 1, the degradation of the amplitude spectrum (in terms of resonances abatement) is also observed at high A_H values, exceeding the threshold values $(A_H)_{th}$ (Figure 5). In particular, in the amplitude spectrum obtained at the value $A_H = 18\,m$, which corresponds to the observed fluctuations in ice thickness on the Ward Hunt Ice Shelf, starting from the impact periodicity $T \approx 2.5\,s$, there are no resonance peaks in the spectrum (Figure 5).

Figure 6 shows the alignment of the zone of the expected appearance of the first band gap ($k_b^{(1)} \approx 6.28\,km^{-1}$) with the resonant peak in the corresponding range of periodicities of the forcing.

In particular, **(a)** with the amplitude of ice thickness fluctuations A_H equal to $\boldsymbol{5\,m}$ (Fig. 6a), the resonance peak is observed at the periodicity $T_n \approx 32.54\,s$ (i.e. $T_n \approx 32.54\,s$ is one of the eigenvalues), at which the wavenumber in the dispersion spectrum is about $5.84\,km^{-1}$ (i.e. $k_n \approx 5.84\,km^{-1}$); **(b)** with the amplitude of ice thickness fluctuations A_H equal to $\boldsymbol{10\,m}$ (Fig. 6b), the resonance peak is observed at the periodicity $T_n \approx 44.04\,s$, at which the wavenumber in the dispersion spectrum is about $6.16\,km^{-1}$ (i.e. $k_n \approx 6.16\,km^{-1}$); and **(c)** with the amplitude of ice thickness fluctuations A_H equal to $\boldsymbol{12\,m}$ (Fig. 6c), the resonance peak is observed at the periodicity $T_n \approx 55.92\,s$, at which the wavenumber in the dispersion spectrum is about $6.39\,km^{-1}$ (i.e. $k_n \approx 6.39\,km^{-1}$). Respectively, the relative deviation of the corresponding wavenumber k_n from the first *Bragg wavenumber* $k_b^{(1)}$ does not exceed 7%.

The distributions of longitudinal stresses (σ_{xx}) (Fig. 7b; Fig. 8b) reflect the distributions of vertical deformations along the central line of the ice shelf (Fig. 7a; Fig. 8a). That is, the maxima\minima of longitudinal stresses coincide with maxima\minima of vertical deformations in the deformation profile (Fig. 7a and Fig. 7b; Fig. 8a and Fig. 8b). In particular, for a given eigenmode the distribution of longitudinal stresses has a specific periodic structure, in which the maxima\minima are aligned with the antinodes in the mode. Therefore, beyond the band gaps, the longitudinal stress distribution with a specific periodical structure (as in Fig. 7b) is the expected stress distribution in the ice shelf. Vice versa, inside the band gaps the distribution of longitudinal stresses has a quasiperiodic or non-periodic structure (as in Fig. 8b).

The shear stress (σ_{xz}) is an order of magnitude less than the longitudinal stress (Fig. 7c; Fig. 8c). Beyond the band gaps, the maximum\minimum shear stress is usually observed at the grounding line, where in the models the ice shelf was considered rigidly fixed (Fig. 7c). Within the band gaps, the maximum\minimum shear stress is in most cases achieved in a vicinity of ice shelf terminus, since the incident wave does not penetrate deeply into the ice shelf (Fig. 8c).

DISCUSSION AND CONCLUSIONS

(1) All suggested models reveal Bragg scattering for an ice shelf with a rolling surface morphology. The modelled Bragg scattering is expressed in the appearance of the anticipated band gaps in the dispersion spectra.

In Konovalov (2023a) it was established that there is a threshold value of crevasses depth, at which the first band gap (corresponding to the first Bragg wavenumber) appears in the spectra. For ice shelf with rolling surface morphology, the double amplitude of ice thickness oscillations A_H is a parameter similar to the crevasse depth in a crevasse-ridden ice shelf (Freed-Brown et all, 2012). Accordingly, the threshold value of the amplitude $(A_H)_{th}^{(1)}$, at which the expected first band gap appears in the spectrum, also exists for the ice shelf with rolling surface morphology.

Analysis of the superposition of the dispersion spectrum and the amplitude spectrum allowed us to establish the following. The amplitude spectra contain resonance peaks corresponding to wavenumbers that are close to the first Bragg value $k_b^{(1)} \approx 6.28\ km^{-1}$. The appearance of Bragg scattering in a periodic structure, which also moves periodically with the same frequency, implies that the Bragg wavelength ($\lambda_b^{(i)}$) and the amplitude of oscillations of the periodic structure (a) satisfy the condition:

$$a \ll \lambda_b^{(i)}. \qquad (14)$$

In other words, equation (14) is the condition for the occurrence of the expected Bragg scattering in a periodically moving structure. Evidently, at resonance, condition (14) is not satisfied. In fact, condition (14) coincides with the condition for applying the wave equation (9).

Failure to satisfy condition (14) occurs not only when $T = T_n$, i.e. when the periodicity of the incident wave coincides with the eigenvalue (when $a \underset{T \to T_n}{\longrightarrow} \infty$), but also when the periodicity of the forcing falls within the periodicity range containing T_n and which is defined by the width of the resonance peak. Therefore, the probability of the alignment of the expected band gap region with the periodicity range, in which the condition (14) is not satisfied, will be higher for a resonant peak with a larger width. The width of the resonance peaks in the amplitude spectra ($A\ vs\ T$) increases with increasing periodicity of the forcing (Konovalov, 2019). Thus, the probability of the alignment is higher for the first Bragg value $k_b^{(1)}$ than for the remaining $k_b^{(i)}, i = 2,3 \ldots$

These conclusions are confirmed by the results obtained in the present study. That is, the threshold value $(A_H)_{th}^{(1)}$ for the appearance of the first band gap is higher than other threshold values $(A_H)_{th}^{(i)}, i = 2,3 \ldots$ In particular, in Model 1 (with $\alpha_1 = 1, \alpha_2 = 0$) $(A_H)_{th}^{(1)} \approx 15m$, but $(A_H)_{th}^{(i)} < 1, i = 2,3,4$; in Model 2 (with $\alpha_1 = 1, \alpha_2 = 0$) $(A_H)_{th}^{(1)} \approx 14m$ and $(A_H)_{th}^{(i)} < 1, i = 2,3,4$; in Model 2 (with $\alpha_1 = 0, \alpha_2 = 1$) $(A_H)_{th}^{(1)} \approx 15m$ and $(A_H)_{th}^{(i)} \approx 2, i = 2,3,4$.

An increase in the amplitude of ice thickness oscillations A_H (as an analogue of half the depth of ice crevasses in a crevasse-ridden ice shelf) yields shift in the resonance peaks (Konovalov, 2021a). Thus, a band gap appears in the dispersion spectrum, if the amplitude of ice thickness oscillations A_H becomes higher than the threshold value $(A_H)_{th}$.

(2) The torsional deformation component in the modes creates additional difficulties in treatment of the dispersion spectra, especially in Model 3, in which this component is observed in any case of the ratio α_1/α_2 (see supplemental file). Essentially, the torsional deformation component yields additional inter-mode spaces (Konovalov, 2021a) in the dispersion spectra. These additional inter-mode spaces respectively provide transitions between torsional strain components in the modes and appear as discontinuities in the dispersion curves. Moreover, these discontinuities differ from the discontinuities accompanying the transitions between the components of the Lamb-type bending deformation in the modes, and can be considered, in particular, as a result of Bragg scattering if these discontinuities are located near the Bragg value. Thus, complementary investigation is required to correctly interpret the discontinuity in the dispersion curve. The investigation is based on the combination of dispersion and amplitude spectra (as shown in Figure 6). Specifically, the discontinuities in the dispersion spectra corresponding to transitions between the torsional strain components in the modes and looking like band gaps, but not corresponding to Bragg scattering of the incident wave, coincide with the resonance peaks in the amplitude spectra (see section 4 in the supplemental file). In other words, these discontinuities, corresponding to transitions between the torsional strain components in the modes, are accompanied by a transition through resonances, while the band gaps corresponding to Bragg scattering are not accompanied by the same transition (see section (1) of this discussion). Thus, this spectral difference allows us to establish the type of discontinuity in the dispersion spectra.

(3) In the models considered in this study, the band gap becomes the dominant effect and abates the resonances in the amplitude spectra if the amplitude of ice thickness oscillations A_H exceeds the threshold value $(A_H)_{th}$. Thus, it can be said that the abatement of the incident wave by ice shelf with rolling surface/base morphology

protects the ice shelf from dangerous resonant impact. For example, the range of periodicities, where the first band gap is observed (Fig. 4a), intersects with the range, where infragravity waves were observed: the range of periodicities is 50..250 s (Bromirski and others, 2010). That is, the first band gap, in particular, can protect the ice shelf from the impact of infragravity waves. This abatement may explain how multiyear sea ice in the Arctic Ocean along the coast of Ellesmere Island can be sufficiently stable and long-lived to evolve into the ice-shelf, once contiguous along the Ellesmere Island coast, reported by European and American explorers in the late 19th and early 20th centuries.

DATA AND RESOURCES

Full descriptions of the three models considered in this study are available on the Zenodo website.

1) Model 1:

   `https://doi.org/10.5281/zenodo.4004338`

   `https://doi.org/10.5281/zenodo.5562017`

2) Model 2:

   `https://doi.org/10.5281/zenodo.7697142`

   `https://doi.org/10.5281/zenodo.10252877`

3) Model 3:

   `https://doi.org/10.5281/zenodo.5761719`

(Last accessed December 2024)

The **supplemental file (SI)** contains the range of results (figures and description) obtained from the experiments performed

ACKNOWLEDGMENTS

I thank prof. Douglas R. MacAyeal for helpful discussion of this manuscript and for the comments to this manuscript that allowed to improve this manuscript. I thank Peter Nekrasov for his assistance in presentation of preliminary results of this study at the AGU Fall Meeting 2022. I thank editors of Annals of Glaciology, Dr. Adrian Jenkins, Dr. Rachel Carr and two referees of this journal for the comments on this manuscript that improved it.

REFERENCES

Ashcroft NW and Mermin ND (1976) *Solid state physics*. Books Cole, Belmont, California

Bennetts LG, Biggs NRT, Porter D (2009) The interaction of flexural-gravity waves with periodic geometries. *Wave Motion*, **46** (1), 57-73 (doi.org/10.1016/j.wavemoti.2008.08.002)

Bennets L, Squire V (2009) Wave scattering by multiple rows of circular ice floes. *J. Fluid Mech.*, **639**, 213-238 (doi:10.1017/S0022112009991017)

Bennets L, Williams T (2010) Wave scattering by ice floes and polynyas of arbitrary shape. *J Fluid Mech.*, 662, 5-35 (doi:10.1017/S0022112010004039)

Bennetts LG, Squire VA (2012) On the calculation of an attenuation coefficient for transects of ice-covered ocean. *Proc. R. Soc. A.*, **468**, 136–162 (doi:10.1098/rspa.2011.0155)

Bennetts LG, Williams TD, Porter R (2024) A thin-plate approximation for ocean wave interactions with an ice shelf. *J. Fluid Mech.*, **984**(A48) (doi:10.1017/jfm.2024.200)

Bromirski PD, Sergienko O, MacAyeal DR (2010) Transoceanic infragravity waves impacting Antarctic ice shelves. *Geophys. Res. Lett.*, **37**, 02502 (https://doi.org/10.1029/2009GL041488)

Bromirski PD, Diez A, Gerstoft P, Stephen RA, Bolmer T, Wiens DA, Aster RC and Nyblade A (2015) Ross ice shelf vibrations. *Geophys. Res. Lett.*, **42**, 7589–7597 (doi:10.1002/2015GL065284)

Cathles LM IV, Okal EA and MacAyeal DR (2009) Seismic observations of sea swell on the floating Ross Ice Shelf, Antarctica. *J. Geophys. Res.*, **114**, F02015 (doi:10.1029/2007JF000934)

Cannata A, Cannavò F, Moschella S and others (2019) Exploring the link between microseism and sea ice in Antarctica by using machine learning. *Sci Rep* **9**, 13050. (https://doi.org/10.1038/s41598-019-49586-z)

Chaput J, Aster RC, McGrath D, Baker M, Anthony RE, Gerstoft P and others (2018). Near-surface environmentally forced changes in the Ross Ice Shelf observed with ambient seismic noise. *Geophys. Res. Lett.*, **45**(11), 187–11,196 (https://doi.org/10.1029/2018GL079665)

Chou T (1998) Band structure of surface flexural-gravity waves along periodic interfaces. *J. Fluid Mech.*, **369**, 333-350 (doi:10.1017/S002211209800192X)

Coffey NB, MacAyeal DR, Copland L and others (2022) Enigmatic surface rolls of the Ellesmere Ice Shelf. *Journal of Glaciology*, **68**(271), 867-878 (doi:10.1017/jog.2022.3)

Dowdeswell JA, Jeffries MO (2017) *Arctic Ice Shelves: An Introduction*. In: Copland L, Mueller D (eds) *Arctic Ice Shelves and Ice Islands*. Springer Polar Sciences, Springer, Dordrecht. (https://doi.org/10.1007/978-94-024-1101-0_1)

Freed-Brown J, Amundson J, MacAyeal D and Zhang W (2012) Blocking a wave: Frequency band gaps in ice shelves with periodic crevasses. *Ann. Glaciol.*, **53**(60), 85-89 (doi: 10.3189/2012AoG60A120)

Guillemot A, Baillet L, Garambois S, Bodin X, Helmstetter A, Mayoraz R and Larose E (2021) Modal sensitivity of rock glaciers to elastic changes from spectral seismic noise monitoring and modeling. *The Cryosphere*, **15**, 501–529 (https://doi.org/10.5194/tc-15-501-2021)

Hattersley-Smith G, Crary AP and Christie RL (1955) Northern Ellesmere Island, 1953 and 1954. *Arctic*, **8**(1), 3–36

Hattersley-Smith G (1957) The rolls on the Ellesmere Ice Shelf. *Arctic*, **10**(1), 32–44

Holdsworth G and Glynn J (1978) Iceberg calving from floating glaciers by a vibrating mechanism. *Nature*, **274**, 464-466

Ilyas M, Meylan MH, Lamichhane B, Bennetts LG (2018) Time-domain and modal response of ice shelves to wave forcing using the finite element method. *J. Fluids and Structures,* **80**, 113-131 (doi:10.1016/j.jfluidstructs.2018.03.010)

Jeffries MO (2017) *The Ellesmere Ice Shelves, Nunavut, Canada*. In: Copland L, Mueller D (eds) *Arctic Ice Shelves and Ice Islands*. Springer Polar Sciences. Springer, Dordrecht. (https://doi.org/10.1007/978-94-024-1101-0_2)

Kalyanaraman B, Bennetts LG, Lamichhane B, Meylan MH (2019) On the shallow-water limit for modelling ocean-wave induced ice-shelf vibrations. *Wave Motion,* **90**, 1-16 (doi: 10.1016/j.wavemoti.2019.04.004)

Kalyanaraman B, Meylan MH, Bennetts LG, Lamichhane BP (2020) A coupled fluid-elasticity model for the wave forcing of an ice-shelf. *J. Fluids and Structures,* **97**, 103074 (doi: 10.1016/j.jfluidstructs.2020.103074)

Konovalov YV (2019) Ice-shelf vibrations modeled by a full 3-D elastic model. *Ann. Glaciol.* **60**(79) 68-74 (doi: 10.1017/aog.2019.9)

Konovalov YV (2020) *Ice-shelf vibrations modeled by a full 3-D elastic model (Program Code) (Ver 2)*. Zenodo (http://doi.org/10.5281/zenodo.4004338)

Konovalov YV (2021a) Abatement of Ocean-Wave Impact by Crevasses in an Ice Shelf. *J. Mar. Sci. Eng.*, **9**, 46 (https://doi.org/10.3390/jmse9010046)

Konovalov YV (2021b) *Ice-shelf vibrations modeled by a full 3-D elastic model (Version#3) (Patent)*. Zenodo (https://doi.org/10.5281/zenodo.5562017)

Konovalov YV (2021c) *Ice-shelf vibrations modeled by a full 3-D elastic model (Version#4) (Patent)*. Zenodo (https://doi.org/10.5281/zenodo.5761719)

Konovalov YV (2023a) Modeling of Ocean Wave Impacts on Crevassed Ice Shelves. *Seismological Research Letters*, **94**(3), 1526–1535 (doi: https://doi.org/10.1785/0220220263)

Konovalov YV (2023b) *Ice-shelf vibrations modeled by a full 3-D elastic model (Version#5) (Patent)*. Zenodo (https://doi.org/10.5281/zenodo.7697142)

Konovalov YV (2023c) *Ice-shelf vibrations modeled by a full 3-D elastic model (Version#6) (Patent)*. Zenodo (https://doi.org/10.5281/zenodo.10252877)

Landau LD, Lifshitz EM (1986) *Theoretical Physics, Vol. 7, Theory of Elasticity*, 3rd edn. Butterworth-Heinemann, Oxford

Lewis CFM, Moore Jr TC, Rea DK, Dettman DL, Smith AJ and Mayer LA (1994) Lakes of the Huron basin: their record of runoff from the Laurentide Ice Sheet. *Quaternary Science Reviews*, **13**, 891–922

Lurie AI (2005) *Theory of Elasticity*. Springer, Foundations of Engineering Mechanics, Berlin.

MacAyeal DR, Okal EA, Aster RC and Bassis JN (2008) Seismic and hydroacoustic tremor generated by colliding icebergs. *J. Geophys. Res.*, **113**, F03011 (doi:10.1029/2008JF001005)

MacAyeal DR, Okal EA, Aster RC, Bassis JN (2009) Seismic observations of glaciogenic ocean waves (micro-tsunamis) on icebergs and ice shelves. *Journal of Glaciology*, **55**(190):193-206 (doi:10.3189/002214309788608679)

MacAyeal D, Sergienko O, Banwell A (2015) A model of viscoelastic ice-shelf flexure. *J. Glaciol.*, **61**(228), 635-645 (doi:10.3189/2015JoG14J169)

MacAyeal DR, Banwell AF, Okal EA and others (2019) Diurnal seismicity cycle linked to subsurface melting on an ice shelf. *Ann. Glaciol*., **60**(79), 137-157 (doi:10.1017/aog.2018.29)

McNeil S, Meylan MH (2023) Time-Dependent Modelling of the Wave-Induced Vibration of Ice Shelves. *J. Mar. Sci. Eng.* **11**, 1191 (https://doi.org/10.3390/jmse11061191)

Mei CC (1985) Resonant reflection of surface water waves by periodic sandbars. *J. Fluid Mech.*, **152**, 315-335 (doi: S0022112085000714)

Meylan M, Bennetts L, Hosking R, Catt E (2017) On the calculation of normal modes of a coupled ice-shelf/sub-ice-shelf cavity system. *J. Glaciol.*, **63**(240), 751-754 (doi:10.1017/jog.2017.27)

Nekrasov P, MacAyeal DR (2023) Ocean wave blocking by periodic surface rolls fortifies Arctic ice shelves. *J. Glaciol.*, 1-11 (doi:10.1017/jog.2023.58)

Newton R, Pfirman S, Tremblay LB and DeRepentigny P (2021) Defining the "ice shed" of the Arctic Ocean's Last Ice Area and its future evolution. *Earth's Future*, **9**, e2021EF001988 (https://doi.org/10.1029/2021EF001988)

Papathanasiou TK, Karperaki AE, Theotokoglou EE and Belibassakis KA (2015) Hydroelastic analysis of ice shelves under long wave excitation. *Nat. Hazards Earth Syst. Sci.* **15**, 1851–1857 (doi:10.5194/nhess-15-1851-2015)

Papathanasiou TK, Karperaki AE, Belibassakis KA (2019) On the resonant hydroelastic behaviour of ice shelves. *Ocean Modelling*, **133**, 11-26 (doi:10.1016/j.ocemod.2018.10.008)

Reeh N Christensen EL, Mayer C, Olesen OB (2003) Tidal bending of glaciers: a linear viscoelastic approach. *Ann. Glaciol.*, **37**, 83–89 (doi:10.3189/172756403781815663)

Rosier SHR, Gudmundsson GH and Green JAM (2014) Insights into ice stream dynamics through modeling their response to tidal forcing. *The Cryosphere*, **8**, 1763–1775 (https://doi.org/10.5194/tc-8-1763-2014)

Pattyn F (2000) Ice-sheet modeling at different spatial resolutions: focus on the grounding zone. *Annals of Glaciology*, **31**, 211-216 (doi:10.3189/172756400781820435)

Pattyn F (2002) Transient glacier response with a higher-order numerical ice-flow model. *Journal of Glaciology*, **48**(162), 467-477 (doi:10.3189/172756502781831278)

Scambos TA, Hulbe C, Fahnestock M, Bohlander J (2000) The link between climate warming and breack-up of ice shelves in the Atlantic Peninsula. *J. Glaciol.*, **46**(154), 516-530 (doi:10.3189/172756500781833043)

Schlindwein VSN, Henning K, Hiller M, Scholz J-R, Schmidt-Aursch MC (2020) First Ocean Bottom Seismometer network underneath the ice-covered Arctic Ocean: Operational challenges and chances for monitoring the state of the sea ice cover. *AGU Fall Meeting 2020*, poster S055-0005.

Sergienko O (2013) Normal modes of a coupled ice-shelf/sub-ice-shelf cavity system. *J. Glaciol.*, **59**(213), 76–80 (doi:10.3189/2013JoG12J096)

Sergienko OV (2017) Behavior of flexural gravity waves on ice shelves: Application to the Ross Ice Shelf. *J. Geophys. Res. Oceans*, **122**(8), 6147–6164 (https://doi.org/10.1002/2017JC012947)

Serripierri A, Moreau L, Boue P, Weiss J and Roux P (2022) Recovering and monitoring the thickness, density, and elastic properties of sea ice from seismic noise recorded in Svalbard. *The Cryosphere*, **16**, 2527–2543 (https://doi.org/10.5194/tc-16-2527-2022)

Sheng P (2006) *Introduction to wave scattering, localization and mesoscopic phenomena*. Springer, Berlin.

Schulson EM (1999) The Structure and Mechanical Behavior of Ice. *JOM*, **51** (2), 21-27 (https://doi.org/10.1007/s11837-999-0206-4)

Tsai VC and McNamara DE (2011) Quantifying the influence of sea ice on ocean microseism using observations from the Bering Sea, Alaska. *Geophys. Res. Lett.*, **38**, L22502, (doi:10.1029/2011GL049791)

Van der Veen CJ (1998) Fracture mechanics approach to penetration of bottom crevasses on glaciers. *Cold Reg. Sci. Technol.*, **27**(3), 213-223 (https://doi.org/10.1016/S0165-232X(98)00006-8)

Van der Veen CJ (2002) Calving glaciers. *Progr. Phys. Geogr.*, **26**(1), 96–122 (doi: 10.1191/0309133302pp327ra)

Walker RT, Parizek BR, Alley RB, Anandakrishnan S, Riverman KL, Christianson K (2013) Ice-shelf tidal flexure and subglacial pressure variations. *Earth and Planetary Science Letters*, **361**, 422–428 (doi: 10.1016/j.epsl.2012.11.008)

List of Figure Captions

Figure 1. The ice-shelf and the cavity profiles considered in the numerical experiments. **1** – ice shelf surface; **2** – ice shelf base; **3** – sea bottom. The amplitude of ice thickness oscillations $A_H = 18\ m$. Spatial periodicity (Δl_r) of the "rolls" is equal to 0.5 km.

Figure 2. The vertical deflections of the ice shelf resulting from the impact of the frontal incident wave were obtained using **Model 2** with the period of forcing $T = 4\ s$ ($T = \frac{2\pi}{\omega}$, ω is the frequency of the forcing) in the case of **(a)** $\alpha_1 = 1, \alpha_2 = 0$ and **(b)** $\alpha_1 = 0, \alpha_2 = 1$.

Figure 3. Dispersion spectra obtained using **Model 2** with $\boldsymbol{\alpha_1 = 1, \alpha_2 = 0}$ for ice shelf geometries differing in the amplitude of ice thickness oscillations A_H (Figure 1): **1** –$A_H = 0\ m$; **2** – $A_H = 10\ m$. The arrowheads on the solid color line (curve 2) indicate the approximate positions of the left and right limits, which approximately define the left and right boundaries of the band gap. The dashed-colored line (in curve 2) indicates the perturbed wavenumber in the band gap. Similar arrowheads were also used in Figure 4 and other figures showing dispersion spectra to indicate of the boundaries of the band gaps.

Figure 4. Dispersion spectra obtained using **Model 2** with $\boldsymbol{\alpha_1 = 1, \alpha_2 = 0}$ for ice shelf geometries differing in the amplitude of ice thickness oscillations A_H (Figure 1): **1** –$A_H = 5\ m$; **2** – $A_H = 10\ m$; **3** –$A_H = 12\ m$; **4** –$A_H = 14\ m$; **5** –$A_H = 18\ m$;

(a) area of the expected first band gap; **(b)** area of the expected second band gap; **(c)** area of expected third and fourth band gaps.

The arrowheads on the solid color lines indicate the approximate positions of the left and right boundaries of the band gap. The dashed-colored lines indicate the perturbed wavenumber in the band gap.

Figure 5. Amplitude spectra obtained using **Model 2** with $\boldsymbol{\alpha_1 = 1, \alpha_2 = 0}$ for ice shelf geometries differing in the amplitude of ice thickness oscillations A_H (Figure 1): **1** –$A_H = 5\,m$; **2** – $A_H = 10\,m$; **3** –$A_H = 12\,m$; **4** –$A_H = 14\,m$; **5** –$A_H = 18\,m$;

(a) area of the expected first band gap (Figure 2,a); **(b)** area of the expected second band gap (Figure 2,b)

Figure 6. Dispersion spectrum and amplitude spectrum, including the area of the expected first band gap, obtained using **Model 2** with $\boldsymbol{\alpha_1 = 1, \alpha_2 = 0}$ for ice shelf geometries differing in the amplitude of ice thickness fluctuations A_H (Figure 1): **(a)** $A_H = 5\,m$; **(b)** $A_H = 10\,m$; **(c)** $A_H = 12\,m$.

Figure 7. (a) Vertical displacement of ice W along the centerline due to the impact of the frontal incident wave. **(b)** Distribution of longitudinal stress (σ_{xx}) in a vertical cross-section of the ice shelf along the centerline. **(c)** Distribution of shear stress (σ_{xz}) in a vertical cross-section of the ice shelf along the centerline. The amplitude of ice thickness oscillations $\boldsymbol{A_H = 10\,m}$, the periodicity of forcing $\boldsymbol{T = 5s}$. These distributions were obtained using **Model 1** with $\boldsymbol{\alpha_1 = 1, \alpha_2 = 0}$.

Figure 8. (a) Vertical displacement of ice W along the centerline due to the impact of the frontal incident wave. **(b)** Distribution of longitudinal stress (σ_{xx}) in a vertical cross-section of the ice shelf along the centerline. **(c)** Distribution of shear stress (σ_{xz}) in a vertical cross-section of the ice shelf along the centerline. The amplitude of ice thickness oscillations $\boldsymbol{A_H = 18\,m}$, the periodicity of forcing $\boldsymbol{T = 5s}$. These distributions were obtained using **Model 1** with $\boldsymbol{\alpha_1 = 1, \alpha_2 = 0}$.

Figures

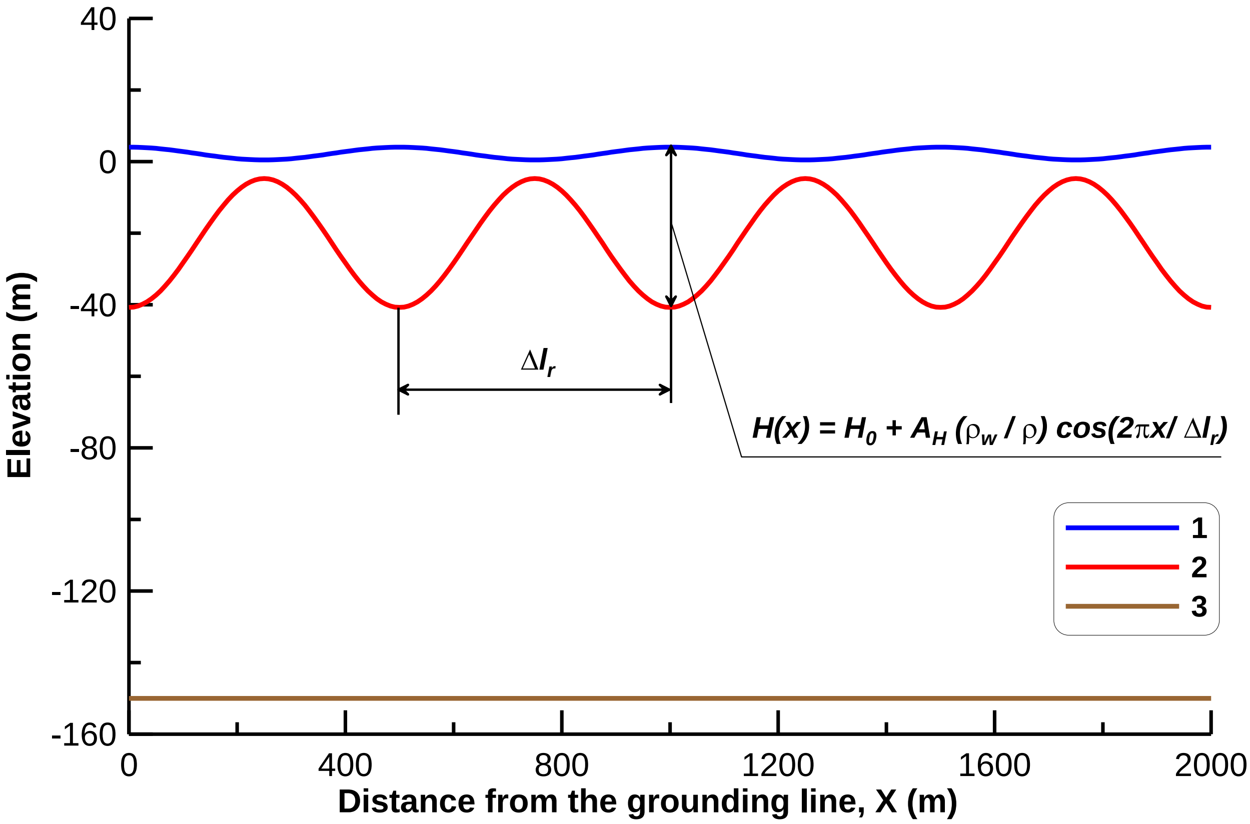

Figure 1. The ice-shelf and the cavity profiles considered in the numerical experiments. **1** – ice shelf surface; **2** – ice shelf base; **3** – sea bottom. The amplitude of ice thickness oscillations $A_H = 18\ m$. Spatial periodicity (Δl_r) of the "rolls" is equal to 0.5 km.

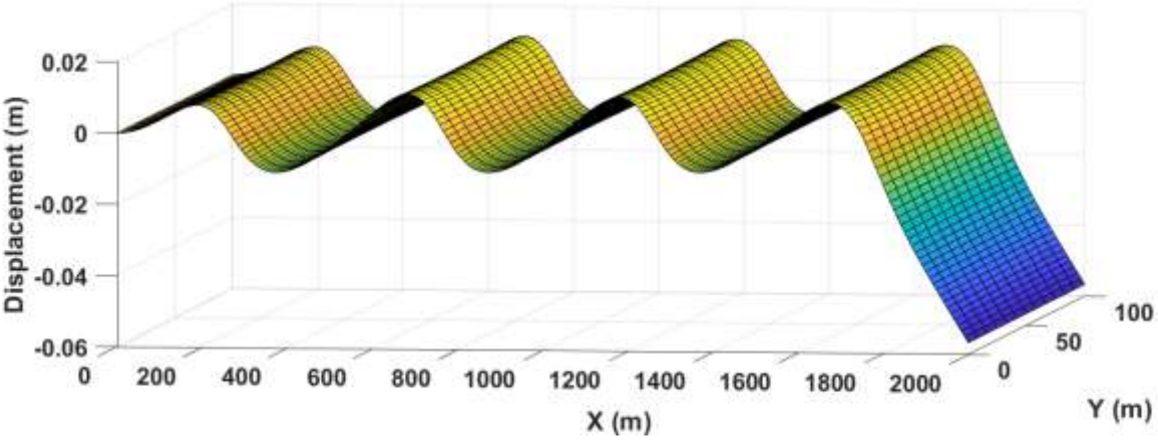

Fig. 2a

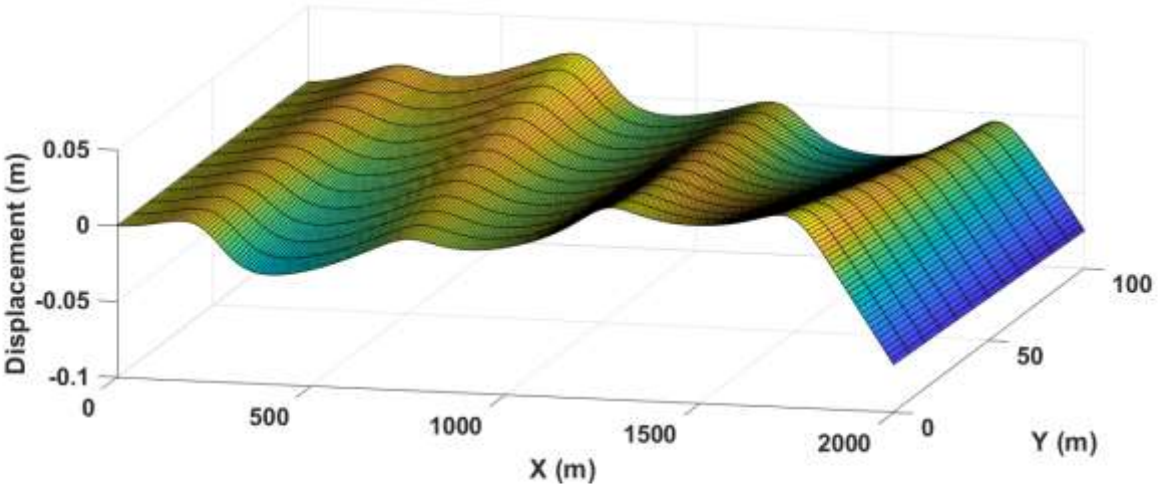

Fig. 2b

Figure 2. The vertical deflections of the ice shelf resulting from the impact of the frontal incident wave were obtained using **Model 2** with the period of forcing $T = 4\ s$ ($T = \frac{2\pi}{\omega}$, ω is the frequency of the forcing) in the case of **(a)** $\alpha_1 = 1, \alpha_2 = 0$ and **(b)** $\alpha_1 = 0, \alpha_2 = 1$.

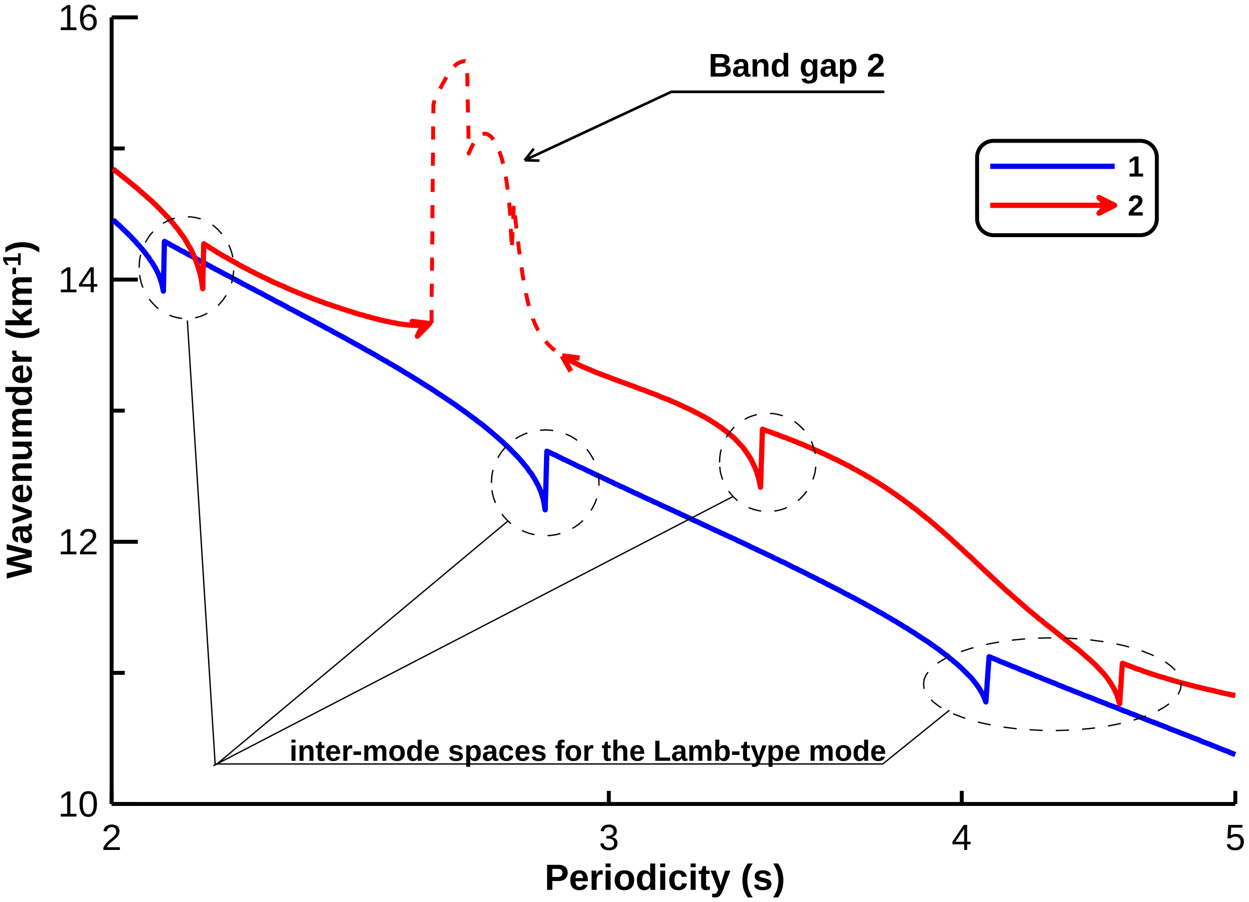

Figure 3. Dispersion spectra obtained using **Model 2** with $\boldsymbol{\alpha_1 = 1, \alpha_2 = 0}$ for ice shelf geometries differing in the amplitude of ice thickness oscillations A_H (Figure 1): **1** $-A_H = 0\ m$; **2** – $A_H = 10\ m$. The arrowheads on the solid color line (curve 2) indicate the approximate positions of the left and right limits, which approximately define the left and right boundaries of the band gap. The dashed-colored line (in curve 2) indicates the perturbed wavenumber in the band gap. Similar arrowheads were also used in Figure 4 and other figures showing dispersion spectra to indicate of the boundaries of the band gaps.

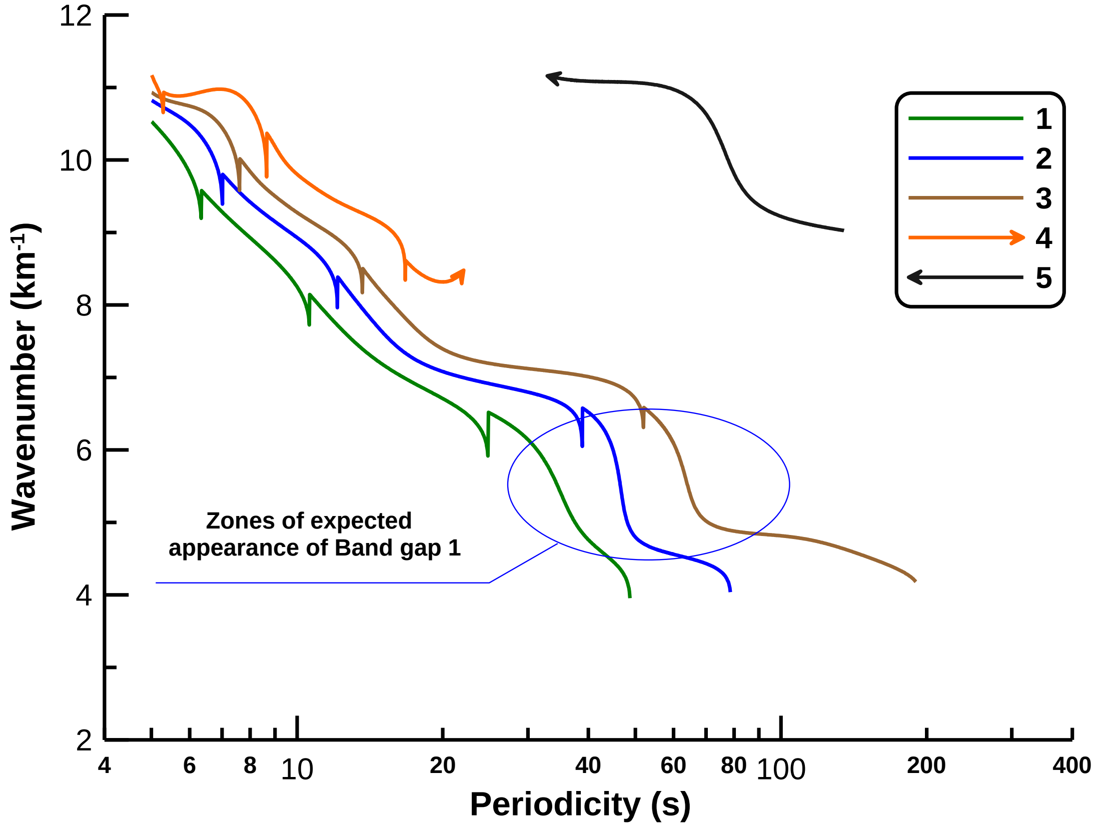
12
10
8
6
4
2
Wavenumber (km^{-1})
4
6
8
10
20
40
60
80
100
200
400
Periodicity (s)
1
2
3
4
5
Zones of expected appearance of Band gap 1

Fig. 4a

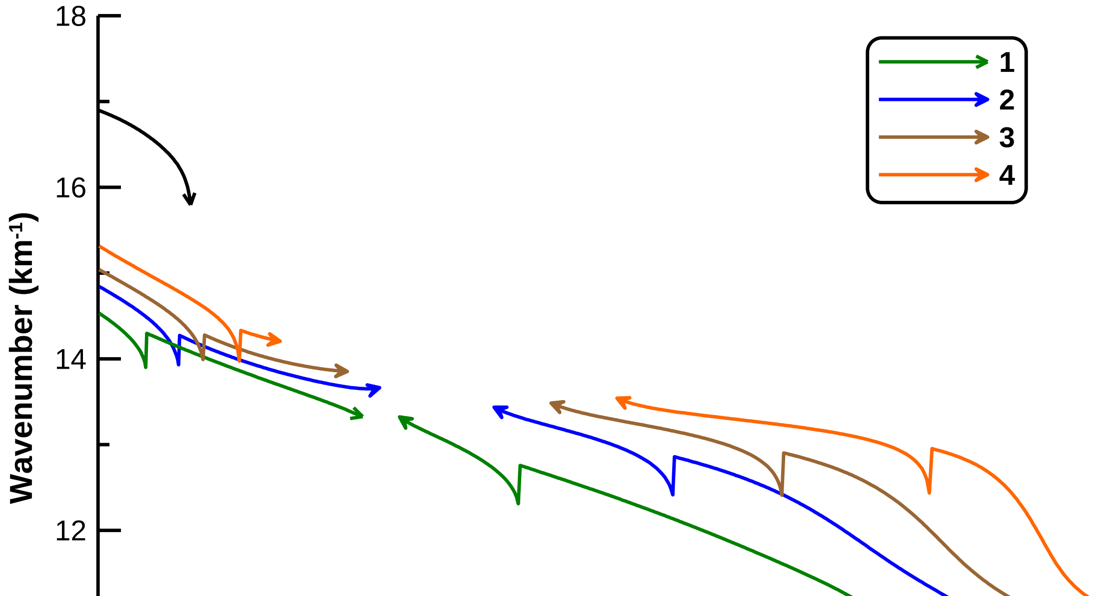
18
16
14
12
10
Wavenumber (km^{-1})
2
3
4
5
Periodicity (s)
1
2
3
4

Fig. 4b

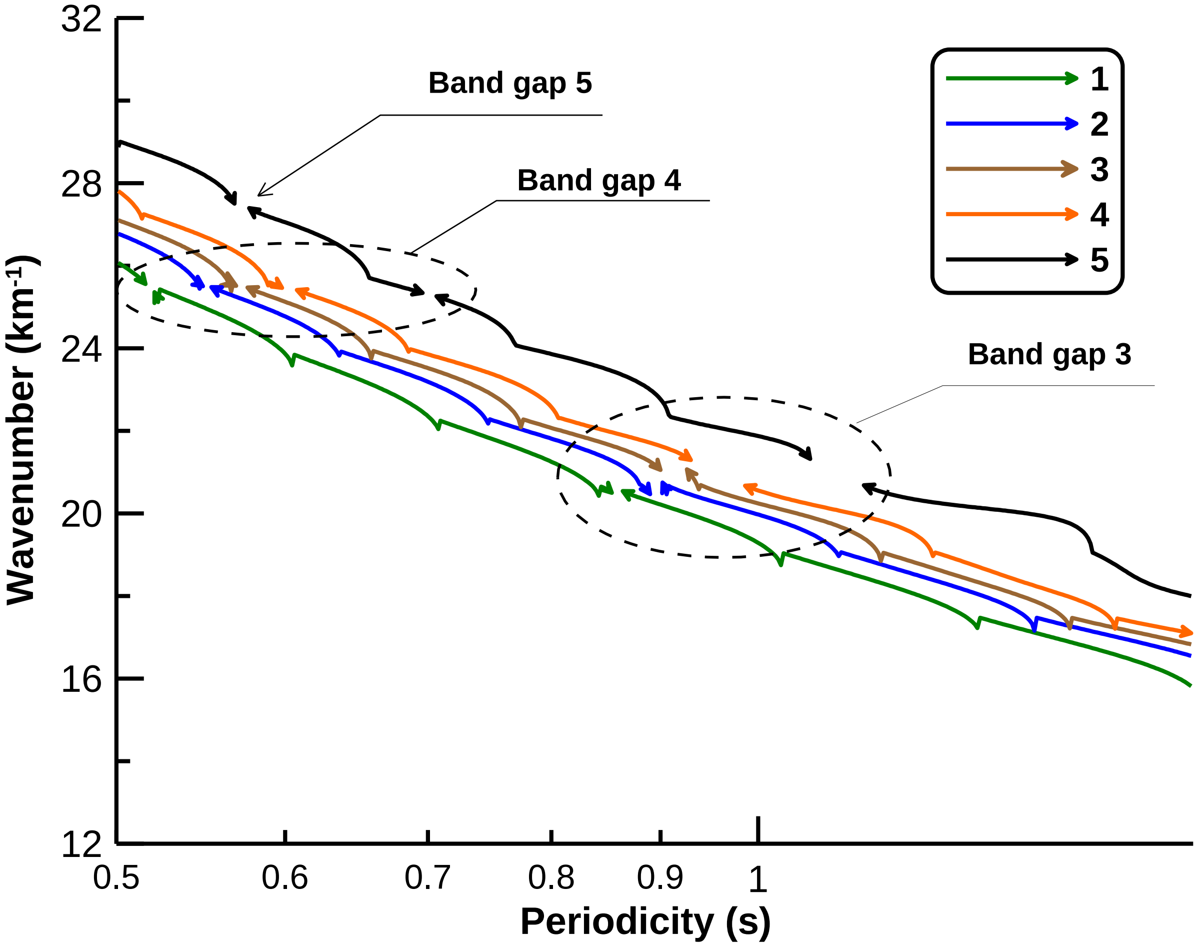

Fig. 4c

Figure 4. Dispersion spectra obtained using **Model 2** with $\boldsymbol{\alpha_1 = 1, \alpha_2 = 0}$ for ice shelf geometries differing in the amplitude of ice thickness oscillations A_H (Figure 1): **1** –$A_H = 5\ m$; **2** – $A_H = 10\ m$; **3** –$A_H = 12\ m$; **4** –$A_H = 14\ m$; **5** –$A_H = 18\ m$;

(a) area of the expected first band gap; **(b)** area of the expected second band gap; **(c)** area of expected third and fourth band gaps.

The arrowheads on the solid color lines indicate the approximate positions of the left and right boundaries of the band gap. The dashed-colored lines indicate the perturbed wavenumber in the band gap.

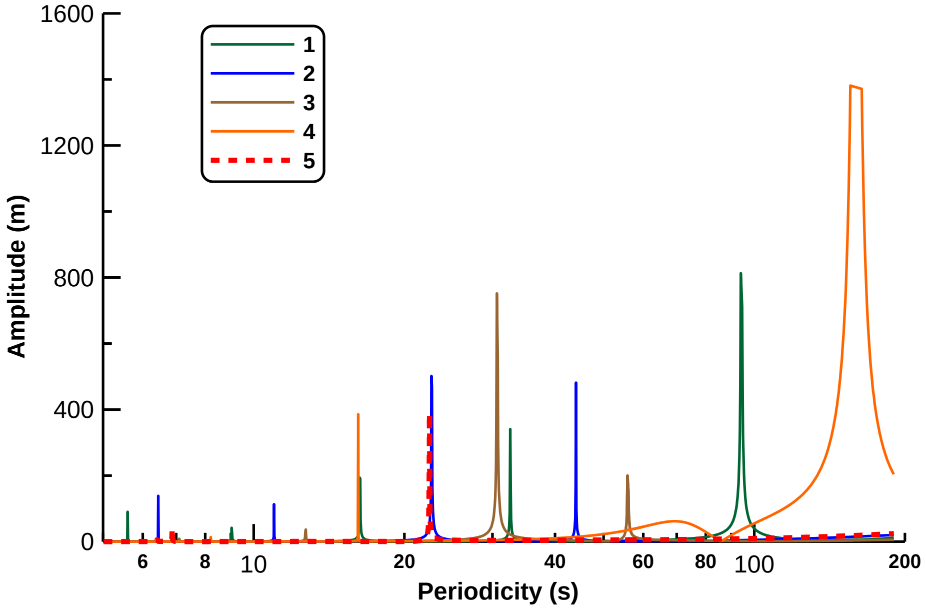

Fig. 5a

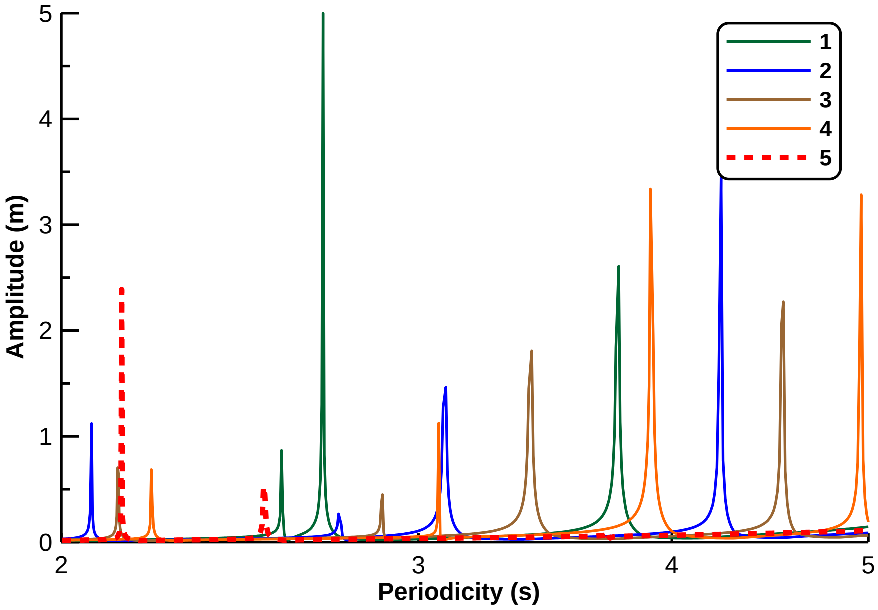

Fig. 5b

Figure 5. Amplitude spectra obtained using **Model 2** with $\boldsymbol{\alpha_1 = 1, \alpha_2 = 0}$ for ice shelf geometries differing in the amplitude of ice thickness oscillations A_H (Figure 1): **1** $– A_H = 5\ m$; **2** $– A_H = 10\ m$; **3** $– A_H = 12\ m$; **4** $– A_H = 14\ m$; **5** $– A_H = 18\ m$;

(a) area of the expected first band gap (Figure 2,a); **(b)** area of the expected second band gap (Figure 2,b)

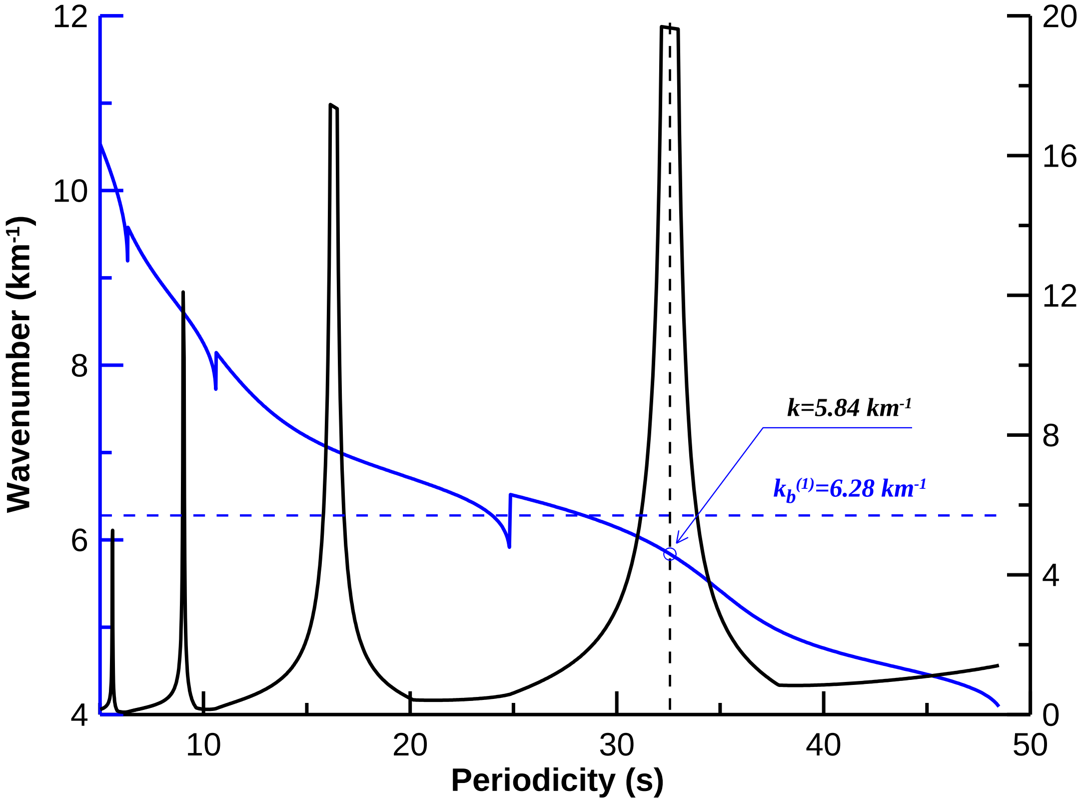
12
10
8
6
4
Wavenumber (km^{-1})
20
16
12
8
4
0
Amplitude (m)
10
20
30
40
50
Periodicity (s)
k=5.84 km^{-1}
$k_b^{(1)}$=6.28 km^{-1}

Fig. 6a

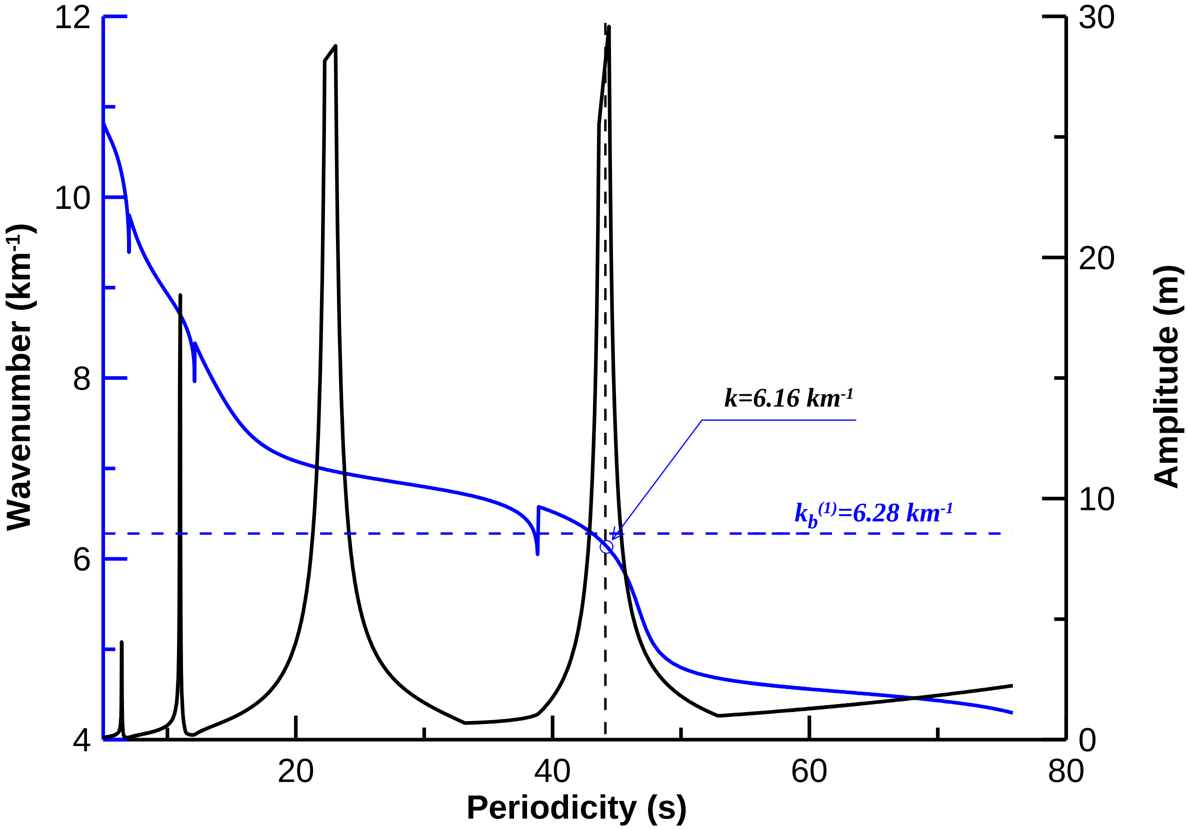
12
10
8
6
4
Wavenumber (km^{-1})
30
20
10
0
Amplitude (m)
20
40
60
80
Periodicity (s)
k=6.16 km^{-1}
$k_b^{(1)}$=6.28 km^{-1}

Fig. 6b

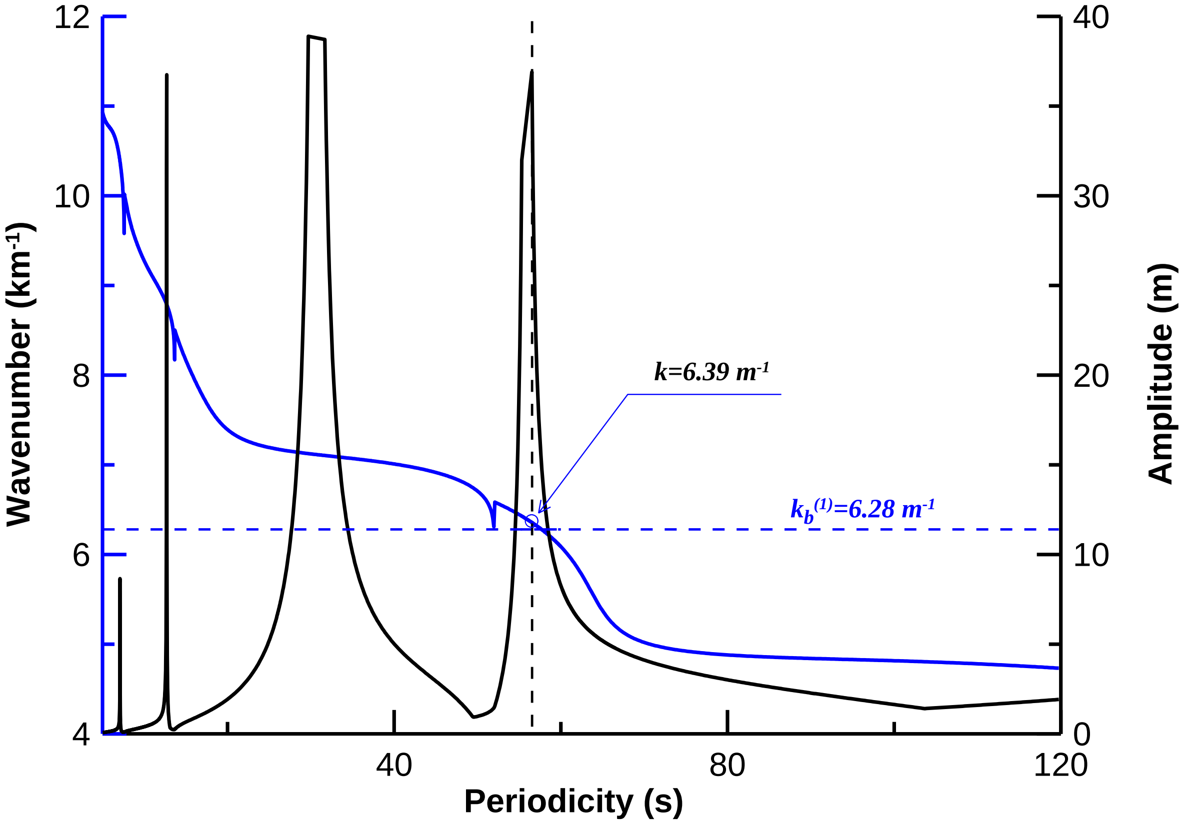

Fig. 6c

Figure 6. Dispersion spectrum and amplitude spectrum, including the area of the expected first band gap, obtained using **Model 2** with $\boldsymbol{\alpha_1 = 1, \alpha_2 = 0}$ for ice shelf geometries differing in the amplitude of ice thickness fluctuations A_H: **(a)** $A_H = 5\,m$; **(b)** $A_H = 10\,m$; **(c)** $A_H = 12\,m$.

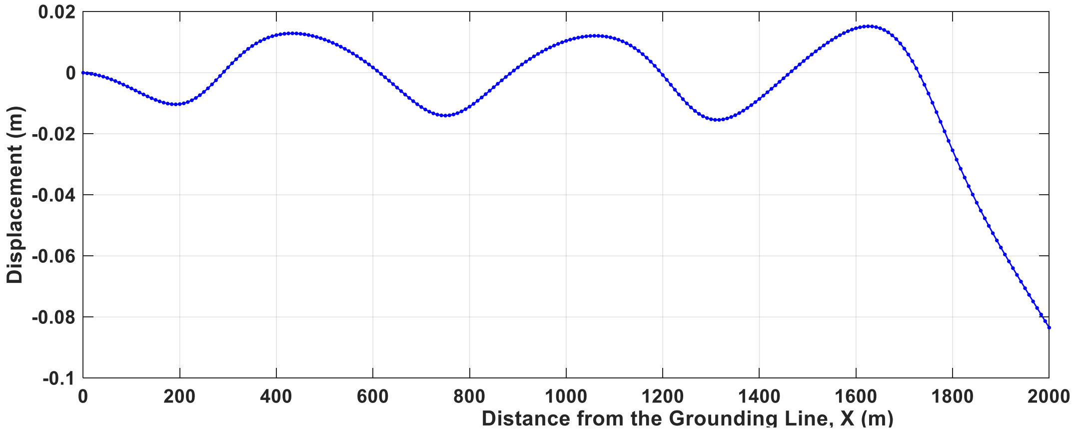

Fig. 7a

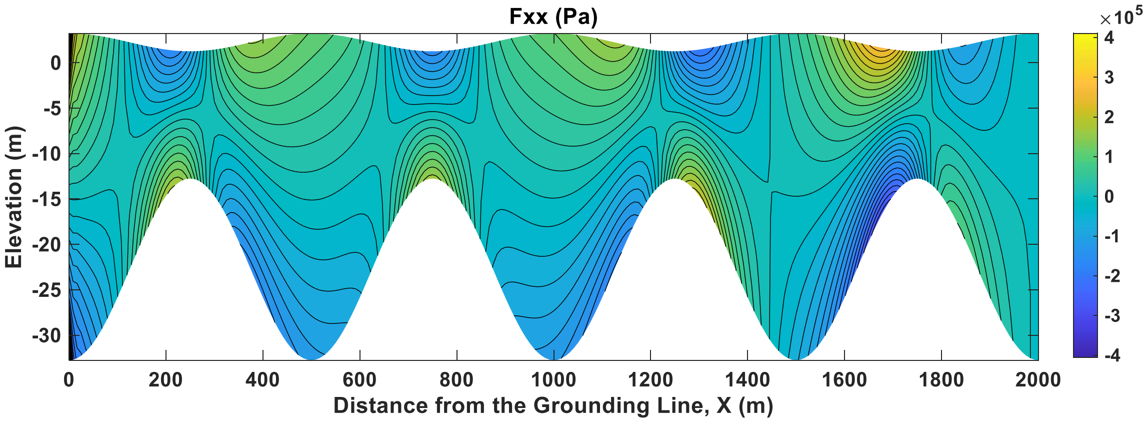

Fig. 7b

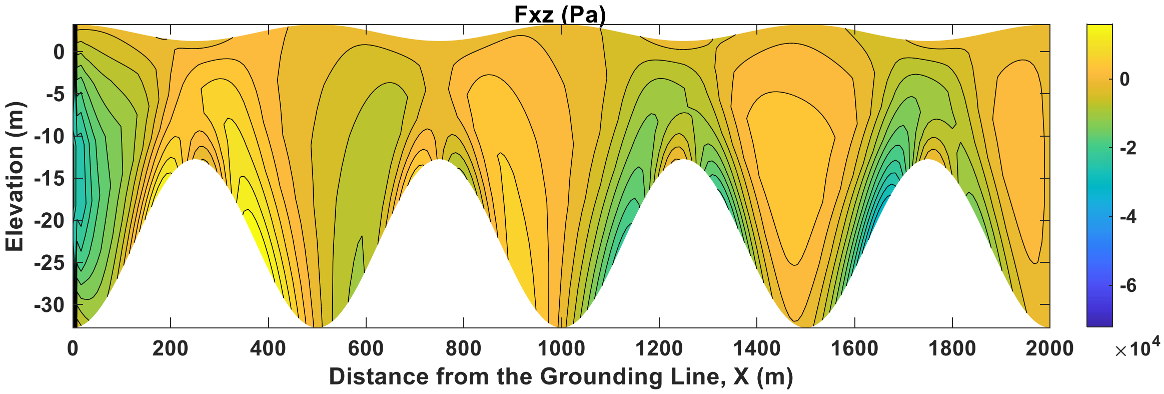

Fig. 7c

Figure 7. (a) Vertical displacement of ice W along the centerline due to the impact of the frontal incident wave. **(b)** Distribution of longitudinal stress (σ_{xx}) in a vertical cross-section of the ice shelf along the centerline. **(c)** Distribution of shear stress (σ_{xz}) in a vertical cross-section of the ice shelf along the centerline. The amplitude of ice thickness oscillations $\boldsymbol{A_H = 10\,m}$, the periodicity of forcing $\boldsymbol{T = 5s}$. These distributions were obtained using **Model 1** with $\boldsymbol{\alpha_1 = 1, \alpha_2 = 0}$.

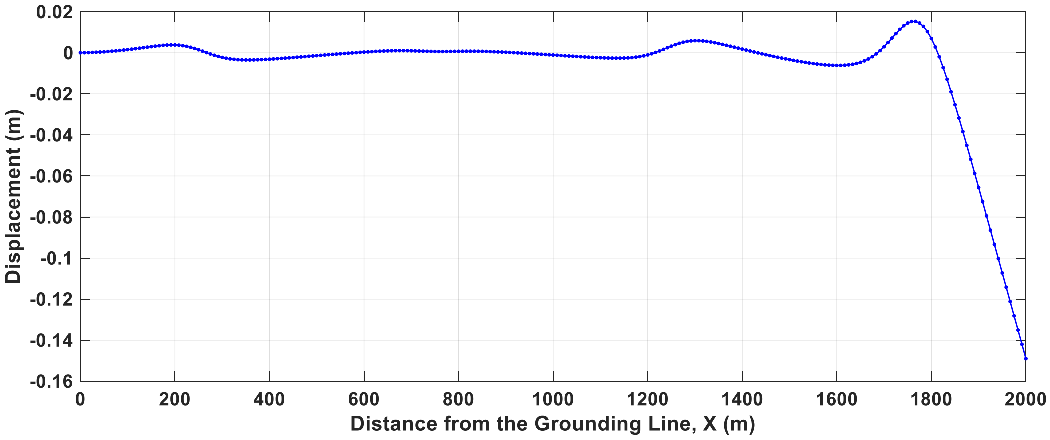
0.02
0
-0.02
-0.04
-0.06
-0.08
-0.1
-0.12
-0.14
-0.16
Displacement (m)
0
200
400
600
800
1000
1200
1400
1600
1800
2000
Distance from the Grounding Line, X (m)

Fig. 8a

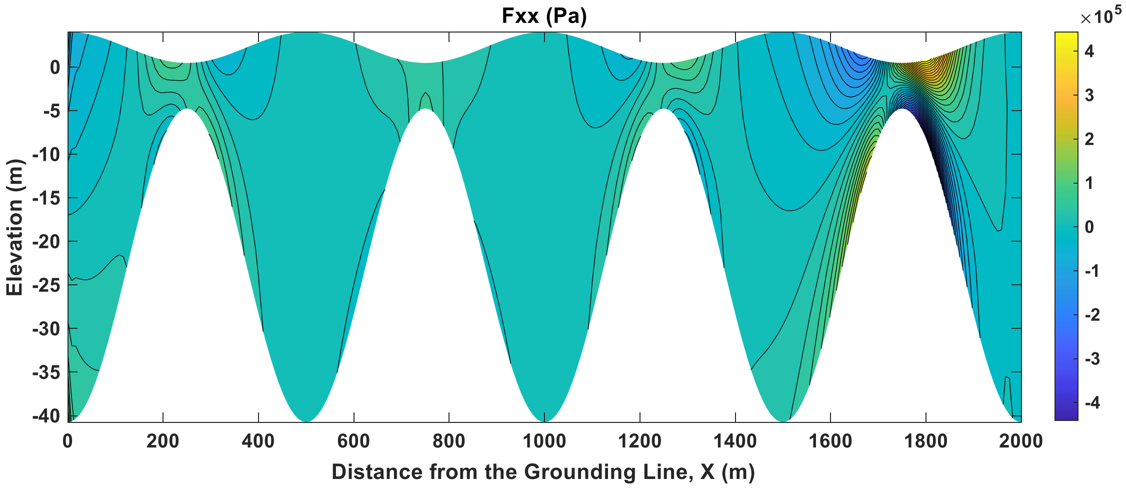
Fxx (Pa)
×10^5
4
3
2
1
0
-1
-2
-3
-4
0
-5
-10
-15
-20
-25
-30
-35
-40
Elevation (m)
0
200
400
600
800
1000
1200
1400
1600
1800
2000
Distance from the Grounding Line, X (m)

Fig. 8b

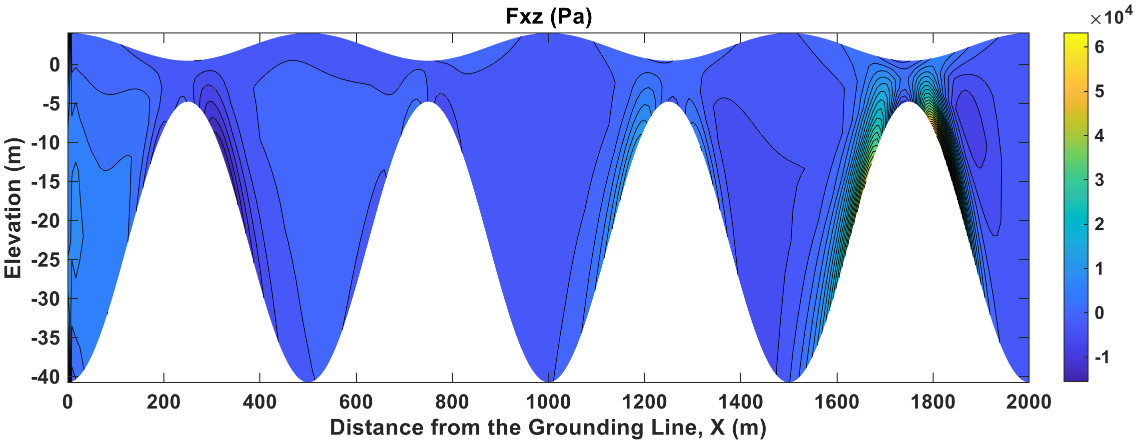

Fig. 8c

Figure 8. (a) Vertical displacement of ice W along the centerline due to the impact of the frontal incident wave. **(b)** Distribution of longitudinal stress (σ_{xx}) in a vertical cross-section of the ice shelf along the centerline. **(c)** Distribution of shear stress (σ_{xz}) in a vertical cross-section of the ice shelf along the centerline. The amplitude of ice thickness oscillations $\boldsymbol{A_H = 18\,m}$, the periodicity of forcing $\boldsymbol{T = 5s}$. These distributions were obtained using **Model 1** with $\boldsymbol{\alpha_1 = 1, \alpha_2 = 0}$.